Journal of Materials Chemistry A

ROYAL SOCIETY OF CHEMISTRY

PAPER

View Article Online
View Journal | View Issue

Cite this: J. Mater. Chem. A, 2024, 12, 28965

$ZnIn_2S_4$ thin films with hierarchical porosity for photocatalysis†

Marco Sigl, [a] Melissa Egger, [a] Fernando Warchomicka, [b] Daniel Knez, [c] Martina Dienstleder, [d] Heinz Amenitsch, [e] Gregor Trimmel [a] and Thomas Rath *[a]

Received 18th June 2024
Accepted 16th September 2024

DOI: 10.1039/d4ta04237a

rsc.li/materials-a

Optimizing the activity of photocatalysts is of great interest for the chemical industry and the renewable energy sector. Zinc indium sulfide is a promising photocatalyst due to its absorption in the visible and UV range and its suitable energy levels. Immobilized heterogeneous catalysts, known for their ease of handling and integration into flow reaction systems, often suffer from low surface areas, limiting reaction sites. To address this, we combined microsphere lithography with a single-source precursor method using metal xanthates to fabricate zinc indium sulfide thin films with hierarchical porosity. The resulting films feature macropores around 300 nm and micropores of approximately 2 nm in diameter. This hierarchical porosity increases the surface area, providing more active catalytic sites and reducing charge transport distances. In dye degradation tests with Rhodamine B, the porous films exhibited specific photocatalytic activity over 3 times higher than for planar films and comparable dispersed powder systems reported in the literature. Our findings suggest that multiscale porosity is a promising strategy for enhancing the activity of photocatalysts.

Introduction

With the growing consumption of energy and the rising demand for environmentally friendly alternatives to fossil fuels, photocatalysis poses an important technology for utilizing the virtually inexhaustible energy from the sun for renewable fuel synthesis. Besides the generation of hydrogen or the reduction of carbon dioxide, photocatalysis provides possibilities to decompose waste materials and to yield chemical reagents.[1–4] Additionally, metal chalcogenides show a promising development in energy storage applications.[5,6] Among the researched photocatalysts, ternary metal chalcogenides like $ZnIn_2S_4$ have received significant attention for their unique properties, like their layered crystal structure and their stability.[7,8]

$ZnIn_2S_4$ (ZIS) shows two crystal phases, a cubic and a hexagonal one, as well as several polytypes of the latter. All polymorphs of $ZnIn_2S_4$ are reported to induce water splitting under visible light with some reports exploring their potential for dye degradation.[9,10] The hexagonal polymorph is thermodynamically stable and shows an indirect bandgap, which is well tuneable from 2.0 to 2.8 eV and conduction band levels of approx. −1.36 to −0.8 eV *vs.* NHE,[4,8,11–16] thereby having good visible light absorption and also fulfilling the energetic requirements for applications such as water splitting. The aforementioned polytypes are based on the stacking of packets of S–Zn–S–In–S–In–S layers.[8,17–19]

For photocatalytic applications, the morphology of the materials is very important to provide a large surface area and fast charge transport. In literature, many reports can be found describing different morphologies of $ZnIn_2S_4$ nanomaterials ranging from zero-dimensional nanocrystals,[20] one-dimensional nanowires and -tubes,[21] two-dimensional sheet-like structures[16,22,23] and three-dimensional (*e.g.* nanoflower-like) structures.[3,9,14,24–26] Because of its layered structure, $ZnIn_2S_4$ tends to form 2D structures, which can be assembled to 3D structures. Chen *et al.* for example employed marigold-like spherical superstructures, composed of numerous nanosheets for photocatalytic dye degradation.[9] This distinctly increases the accessible surface and thus the available active sites.

A different approach for increasing the photocatalytic activity is the deployment of co-catalysts. Combining $ZnIn_2S_4$ with a co-catalyst can improve the separation of photogenerated

[a]Institute for Chemistry and Technology of Materials, NAWI Graz, Graz University of Technology, Stremayrgasse 9, 8010 Graz, Austria. E-mail: thomas.rath@tugraz.at
[b]Institute of Materials Science, Joining and Forming, Graz University of Technology, Kopernikusgasse 24, 8010 Graz, Austria
[c]Institute of Electron Microscopy and Nanoanalysis, Graz University of Technology, Steyrergasse 17, 8010 Graz, Austria
[d]Austrian Centre for Electron Microscopy and Nanoanalysis, Steyrergasse 17, 8010 Graz, Austria
[e]Institute of Inorganic Chemistry, NAWI Graz, Graz University of Technology, Stremayrgasse 9, 8010 Graz, Austria

† Electronic supplementary information (ESI) available: Additional SEM images, GIWAXS/GISAXS data and videos, XRD, BET adsorption, FT-IR, NMR data, as well as information about the synthetic procedures and the analysis of the X-ray scattering data. See DOI: https://doi.org/10.1039/d4ta04237a

electrons and holes.[27,28] For example, depositing transition metal chalcogenides as co-catalysts on $ZnIn_2S_4$ is reported to improve the photocatalytic H_2 production up to 37 times compared to pristine $ZnIn_2S_4$, if MoS_2 is used as co-catalyst.[29] Moreover, $In(OH)_3$ formed in small amounts on the ZIS surface *via* simple pH adjustment was proposed by Zhao *et al.* to function as co-catalyst.[30] Although $ZnIn_2S_4$ provides an accessible and versatile photocatalyst material, its exploration and application in thin films, especially structured ones, is still scarce,[31–35] even though thin films could be applied as easy recyclable catalysts or integrated in continuous flow systems.

State-of-the-art preparation methods for $ZnIn_2S_4$, such as the hydrothermal approach, offer many options to control the nanomorphology, for example, varying time, temperature and pH value, however, the focus in these synthesis routes is on the preparation of particles.[3,26] While the hydrothermal preparation yields generally lower crystallinity, defect free nanosheets have been obtained *e.g.* by chemical vapor deposition.[36] A reported approach to synthesize $ZnIn_2S_4$ thin films is the electrodeposition on an electrode, which offers the benefits of short reaction times and low temperature. A drawback however, is the necessity of a subsequent thermal treatment to convert the precursors into the metal sulfide, typically requiring high temperatures (500 °C).[37,38]

Metal xanthates are versatile precursors for the preparation of metal sulfides, the temperatures needed to convert the precursors to the metal sulfides are comparably low and no additional sulfur source has to be added.[39–49] Furthermore, the metal xanthate route offers the possibility to easily prepare the metal sulfides as thin films, unlike the hydrothermal synthesis approaches.[3,26] While the preparation of various ternary metal sulfides has already been demonstrated,[39–43] the formation of $ZnIn_2S_4$ has not been shown yet *via* this approach. Moreover, the metal xanthate route offers unique possibilities to tune the surface morphology and porosity of the obtained films by combining it with structuring methods such as soft-templating or lithographic approaches and the possibility of inherent micropore formation during the conversion to the metal sulfide, which can be tuned by the chemical structure of the xanthates.[50]

In this work, we investigated the preparation of hierarchically porous $ZnIn_2S_4$ thin films *via* metal xanthate precursors as an effective method to improve the photocatalytic activity of $ZnIn_2S_4$. By introducing hierarchical porosity, we can significantly increase the surface area and thus the available active sites for catalytic reactions. At the same time, increasing the surface area also helps reducing the necessary charge transport distances in the material. To obtain such structured thin films, we followed the novel approach of combining macropores originating from microsphere lithography[51,52] with additional micropores that intrinsically form during the conversion process of the xanthate precursor to the metal sulfide,[50] thus introducing multiscale porosity to the material. Moreover, we highlight the positive influence of the introduced porosity in photocatalytic dye degradation experiments.

Results and discussion

Preparation of the microsphere templates

We prepared polystyrene microsphere templates (PS-MS) on silicon substrates as described in the literature for the fabrication of macropores in the metal sulfide films.[51,52] In brief, a polystyrene bead layer (bead diameter: 300 nm) was prepared at the surface of a water/ethanol solvent mixture as shown in Fig. S3, ESI.† The tightly packed two-dimensional layer was transferred onto silicon substrates by lifting it up from the interface with the substrate. By fulfilling the Bragg condition,[52,53] the obtained PS-MS templates show a blue shimmering structural colour.

To create space between the tightly packed spheres for the infiltration of the metal xanthate solution, we treated the PS-MS films with an O_2 plasma to isotropically reduce the sphere sizes. This provides a facile way to homogeneously control the mean size of the beads in the template between 300 and 260 nm and thus the later size of the macropores and the wall thicknesses of the metal sulfide film as presented in Fig. S4, ESI.†

Formation of the $ZnIn_2S_4$ macropores

After the O_2 plasma treatment, the template films were infiltrated by a precursor solution containing a mixture of indium and zinc xanthates acting as zinc, indium, and sulfur sources for the formation of zinc indium sulfide. For this purpose, zinc *O*-pentan-1-yl dithiocarbonate and indium *O*-2,2-dimethylpentan-3-yl dithiocarbonate were successfully synthesized in two steps according to previously reported methods.[50,52,54,55] The synthetic procedure and characterization data are summarized in the ESI.† The alkyl chains in the xanthates (In: 2,2-dimethylpentyl; Zn: pentyl, Fig. 1), were chosen as they provide a good solubility of a mixture of them in various solvents unlike smaller alkyl groups like methyl and ethyl. A challenge, however, was that they show the highest solubility in solvents like chloroform and dichloromethane, which unfortunately also dissolve the polystyrene beads in the template and are not soluble in highly polar solvents like water or ethanol. Based on previous studies from our group, investigating the use of metal xanthates to prepare nanostructured metal sulfide films for application in hybrid solar cells[56] and honeycomb structured copper indium sulfide[52] thin films, the metal xanthates were dissolved in ternary solvent mixtures consisting of various amounts of dichloromethane (DCM), ethanolamine (EtA) and either ethanol (EtOH) or 2-propanol (iPrOH); see Table S1† for more details. In this study, the most successful infiltration and consequently macropore formation was achieved with a 20 : 10 : 1 EtOH : DCM : EtA mixture (vol : vol : vol, in the following referred to as EDE), with which the following experiments were conducted.

We performed the infiltration of the template films by dropping the precursor solution on the templates followed by a soaking period of 10 s before removing excess solution *via* spin coating (5000 rpm), as depicted in Fig. 1. The infiltrated templates were dried at room temperature in N_2 atmosphere for 15 minutes. This was followed by another drying step at 90 °C

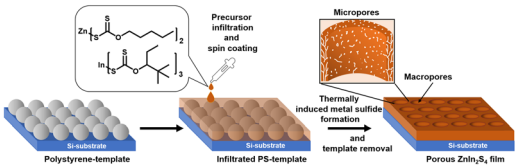

Fig. 1 Preparation of the hierarchically porous $ZnIn_2S_4$ thin films comprising macropores and micropores.

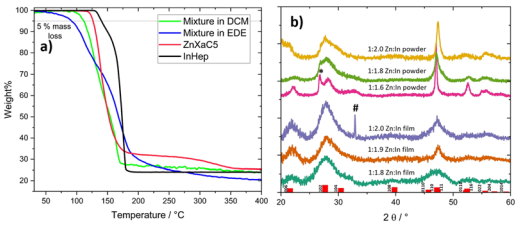

Fig. 2 (a) TGA measurements of the individual precursors and mixtures. (b) Diffractograms of $ZnIn_2S_4$ powder samples as well as thin films on silicon wafer substrates with a hexagonal $ZnIn_2S_4$ reference (red – PDF 65-2023). The annealing temperature was 400 °C; * marks the prominent 100 reflex of ZnS (COD 9008878) in the indium-poor mixture (Zn : In = 1 : 1.6); # peak from the silicon substrate. The diffraction patterns are shifted vertically for better visibility.

Table 1 Average macropore sizes of the structured thin films and information about the used solvent and plasma etching time

Solvent mixture	O_2 etching time/min	Pore diameter/nm	Wall thickness/nm
EDE	10	304 ± 43	48 ± 16
EDE	15	289 ± 48	61 ± 23

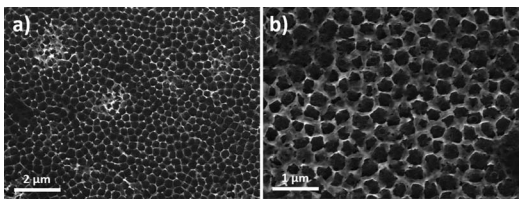

Fig. 3 SEM images of structured films using EtOH : DCM : EtA (20 : 10 : 1) as solvent with 10 min O_2 plasma treatment at (a) 25k× and (b) 50k× magnification.

for 30 minutes to remove the remaining solvents, as they interfere with the desired $ZnIn_2S_4$ formation.

As we could observe *via* thermogravimetry (Fig. 2a), the individual xanthates start to thermally decompose (5% mass loss) at 126 °C (Zn xanthate) and 140 °C (In xanthate). Notably, for the dissolved Zn- and In-xanthate mixtures (molar ratio of 1 : 2, in DCM or the EDE solvent mixture), the decomposition starts at significantly lower temperatures. The mixed xanthate sample prepared using DCM as solvent showed 5% mass loss already at 111 °C. The decomposition of the EDE-prepared sample shows no clear onset and the value of 5%-mass loss is already reached at 92 °C. This is related to the fact that amines can induce the conversion of the metal xanthates to their respective sulfides already at room temperature.[39] We also observed that the processability of the EDE-solvent based precursor solution containing EtA was limited to 10–15 min. The weight losses of the zinc and indium xanthate as well as the blend of both xanthates prepared from DCM match very well with the theoretical values (see Table S2†). The blend prepared from the EDE solvent mixture revealed a slightly higher mass loss due to EtA partly remaining in the sample due to its high boiling point. In addition, the TGA data reveal that even though the main decomposition steps of the used xanthates and their blends are finished below 200 °C, in particular the blend prepared from the EDE solvent mixture shows continued mass loss up to temperatures of almost 400 °C. Therefore, for the preparation of the structured thin films, after the drying steps (at 90 °C), we heated the films to 400 °C and held this temperature for 5 hours to form the hexagonal ZIS. The higher temperatures, on the one hand, fully convert the xanthate precursors, while also inducing an increased crystallinity and, on the other hand, also serve to remove the polystyrene template from the film. Diffractograms of samples with different Zn : In molar ratios in powder and thin film form are shown in Fig. 2 together with a reference pattern for hexagonal $ZnIn_2S_4$ (PDF 65-2023). In general, $ZnIn_2S_4$ is already formed after a much shorter time at 400 °C as revealed by the XRD pattern shown in Fig. S5† (acquired after 30 min heating at 400 °C), however, the material becomes significantly more crystalline by the longer temperature treatment.

Indicated by the powder samples in Fig. 2, a Zn to In ratio of 1 : 2.0 leads to $ZnIn_2S_4$ as the XRD pattern reveals the typical peaks of hexagonal $ZnIn_2S_4$ at 2θ values of 21.6°, 27.7°, 47.2° as well as the multiple peaks between 52.2 and 59.2° 2θ and SEM-EDX spectra (Fig. S6, ESI†) reveal a composition of Zn : In : S of 1.00 : 1.99 : 3.54, which is very near to the expected theoretical composition. With reduced indium content, a shoulder at 26.8° 2θ becomes prominent indicating the formation of ZnS as secondary phase in the In-poor samples. Similar to many literature reports, the 108 reflex at 39.8° 2θ, was hardly observed in any of the samples.[3,18,19,57,58] Moreover, we found that in In-rich samples (with Zn : In molar ratios of *e.g.* 1 : 2.2), In_2S_3 is formed in considerable amounts in addition to the $ZnIn_2S_4$ phase and ZnS as a further phase cannot be ruled out (see Fig. S7†). Thus, we used a slightly In-poor ratio (Zn : In = 1 : 1.8) for the preparation of the samples for the further characterizations and photocatalytic experiments. For a comparison, the binary sulfides formed by the individual precursors are depicted in Fig. S8 of the ESI.† From the Scherrer equation, we estimate the primary crystallite size to be 2.0 to 2.2 nm.

In contrast to electrochemically deposited Zn, In and S precursor films as reported by Yu *et al.*,[37] annealing at higher temperatures than 400 °C does not lead to better formation of hexagonal $ZnIn_2S_4$ using the xanthate precursor method. On the contrary, at higher temperatures, the formation of In_2O_3 becomes very prominent (Fig. S9†).

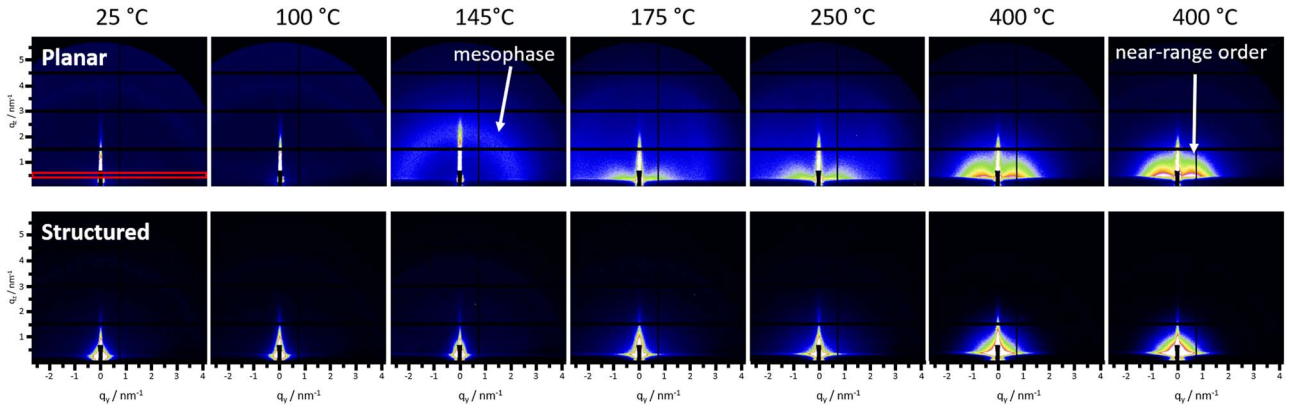

Fig. 4 GISAXS patterns of the heating runs for the $ZnIn_2S_4$ planar film (top) and structured film (bottom) for selected temperatures from 25 °C to 400 °C and after holding the temperature at 400 °C for 15 minutes (right image). The red box in the first image represents the area used for the calculation of the in-plane cuts around q_z of 0.5 nm^{-1}.

Investigation of the thermal conversion to the metal sulfide

The temperature at which $ZnIn_2S_4$ is formed is crucial for the preparation of the macropores *via* the PS-MS template, as a stable metal sulfide film has to be obtained before the deformation and subsequent decomposition of the PS beads. Thus, we characterized the conversion of the metal xanthate precursors to the sulfides with time resolved GIWAXS measurements using synchrotron radiation. The GIWAXS investigations were performed with a planar thin film (without PS-MS templates) from DCM solution on silicon substrates.

At lower temperatures during the heating run (Fig. S10†), we can observe a broad peak at low 2θ values around 15°. This peak diminishes in intensity with increasing temperature. At around 125 °C, this peak cannot be recognized anymore and a broad peak at 31.7° 2θ emerges in the GIWAXS pattern and becomes more clearly visible with increasing temperature. This reveals that a crystalline metal sulfide is formed already at temperatures above 125 °C, which is below the deformability and far below the decomposition temperature of the PS template[59] allowing the formation of a stable metal sulfide film within a well intact template.

Furthermore, this peak becomes narrower and shifts to lower 2θ values. The peak shift from 31.7 to 29.1° 2θ suggests an initial formation of ZnS, which is converted to $ZnIn_2S_4$ at higher temperatures (between 150 and 175 °C). The zinc xanthate decomposes already at lower temperatures than the In xanthate counterpart as revealed by the TGA data (Fig. 2a), supporting an initial ZnS formation. The 101 reflection of hexagonal ZnS appears at 2θ of 30.6° (COD 9008878), the 111 reflection of the cubic phase at 2θ of 28.9° (COD 5000088) and the 102 reflection of $ZnIn_2S_4$ appears at 2θ of 27.7° (PDF 65-2023). Due to the holding time at 400 °C of only 30 min at the end of the heating run for the GIWAXS investigations, the crystallization process is not fully completed, as revealed by the XRD investigations. Therefore, we recorded additional XRD-patterns at different temperatures and times (Fig. S11, ESI†). They confirm this assumption and further reveal that for longer temperature treatment at 400 °C, the discussed peak shifts even more to lower 2θ values. After 5 h at 400 °C the peak shifted to 27.7° 2θ and can be assigned to the 102 reflection of the hexagonal $ZnIn_2S_4$ (Fig. 2 and S11†).

Macropore characterization

In a next step, we characterized the macropores resulting from the PS-MS templates with scanning electron microscopy. Important parameters for the formation of the honeycomb structured macropores were the amount of precursor solution and the solvents used. We found 10 s of infiltration time to be beneficial for the solution to enter the interstitial sites of the template, without significant evaporation of the solvent mixture occurring. The subsequent thermal conversion of the xanthates was carried out at 400 °C in inert atmosphere. The resulting average values of the macropore diameter and wall thickness are listed in Tables 1 and S3 in the ESI† for the mixtures containing 2-propanol instead of ethanol. As expected, when using less time in the O_2 plasma, the pores are larger. Although the standard deviation is rather high due to the comparably large size distribution of the beads, the decrease in diameter and increase in wall thickness match each other very well. Within the investigated solvent mixtures, the most uniform infiltration and macropore formation was observed using the EtOH : DCM : EtA solvent mixture in combination with 10 min of etching time (Fig. 3). The beneficial properties of this solvent mixture arise from a good wettability and infiltration together with a low tendency of dissolving the template. The wall thicknesses were determined at the narrowest position between two pores. In the case of the EDE mixture, these wall thicknesses were 48 and 61 nm (10 and 15 min, Table 1), matching the size and space between the respective PS-spheres very well (Fig. S4, ESI†). The pore-diameters and wall-thicknesses for other investigated solvents are summarized in Table S3.† The film thicknesses, obtained by surface profilometry, are between 80 and 110 nm. In addition, a SEM image of a cross section of a structured $ZnIn_2S_4$ film prepared using the EtOH : DCM : ETA solvent mixture is shown in Fig. S13.† Moreover, for example, when using iPrOH : DCM : EtA in a 4 : 2 : 1 ratio (PDE1, Fig. S14a and

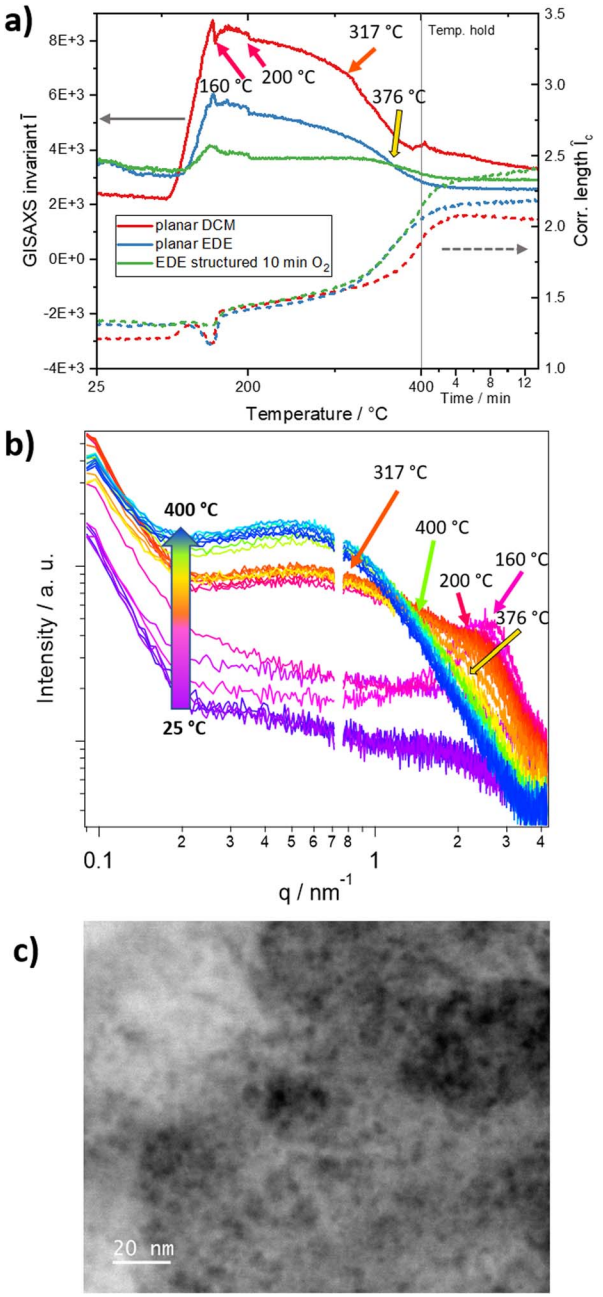

Fig. 5 (a) GISAXS invariant $\bar{I}$ and in-plane correlation lengths $\hat{\xi}_c$ of the planar and structured thin films (q range from 0.1 to 4.18 nm^{-1}); (b) GISAXS in-plane curves during the heating run of the planar DCM thin film in the temperature range from 25 to 400 °C in 25 °C intervals. Significant features and temperatures are marked with matching coloured arrows in (a) and (b) and are discussed in the text. The line-cuts were integrated in a range of $q_{min} = 0.1$ to $q_{max} = 4.18$ nm^{-1}, as marked with the red box in Fig. 4. (c) STEM HAADF image of the nanopores in the $ZnIn_2S_4$ film.

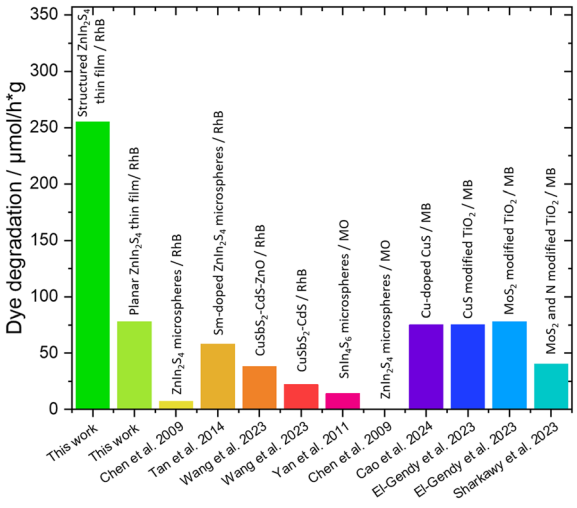

Fig. 6 Specific photocatalytic activity towards the dye degradation of Rhodamine B in this work and with similar metal sulfide-based systems found in the literature.

b, ESI†), there is barely any wettability (due to the high amount of EtA) to the PS-MS and the precursor hardly infiltrated the more narrow spaces. Reducing the amount of ethanolamine to a ratio of iPrOH : DCM : EtA 20 : 10 : 1 (PDE2, Fig. S14c and d, ESI†), the pores become less circular. However, a very interesting aspect of this solvent mixture was that very thin wall thicknesses of around 22 nm were obtained.

Characterization of the micropores (GISAXS)

Referring to previously reported mesoporous metal sulfides based on the decomposition of zinc xanthates, the smaller pores are expected to be in the lower nm range.[50] As this size regime is not accessible *via* SEM measurements, we used GISAXS measurements to determine the sizes of the smaller pores. Similar to the GIWAXS investigations, we also performed a heating run to obtain time-resolved GISAXS data of the conversion from the precursor film to the metal xanthate film. The GISAXS data of the planar film during the heating run (Fig. 4 top row & Fig. 5) reveal at a temperature of approx. 140 °C a low intensity semicircle indicating the formation of an ordered mesophase (third image in the upper row of Fig. 4). The semicircle increases in intensity before almost disappearing again slightly above 160 °C. This can be also very well observed by the ESI Video 1† (ESI, development of the GISAXS images over time during the heating run). As revealed in a previous study, this ordered mesophase is typically formed by decomposition products (mainly alkenes and alcohols) of the metal xanthates and influences the formation of the micropores in the metal sulfide films.[50,60] These decomposition products remain within the film for a certain time after the initial xanthate decomposition without immediate evaporation.

At temperatures above 160 °C, the overall scattering becomes significantly more intense due to the particle growth and the evaporation of the organic decomposition products from the film. Moreover, the features in the GISAXS pattern (marked with an arrow in Fig. 4, top row, last image) indicate a preferential near range order parallel to the surface, corresponding to a preferred orientation parallel to the substrate. We assume that this is associated to the micropores formed in this preferred orientation.

Table 2 Comparison of specific photocatalytic dye degradation from this work and similar catalysts as well as different organic dyes from the literature; RhB: Rhodamine B, MO: methyl orange, MB: methylene blue

Publication	Catalyst	Dye	μmol h^{-1} g^{-1}
This work	Planar $ZnIn_2S_4$ thin film	RhB	78
This work	Hierarchically porous $ZnIn_2S_4$	RhB	289
Chen *et al.* 2009 (ref. 61)	$ZnIn_2S_4$ microspheres	RhB	7.0
Tan *et al.* 2014 (ref. 62)	Sm-doped $ZnIn_2S_4$ microspheres	RhB	58
Wang *et al.* 2023 (ref. 63)	$CuSbS_2$–CdS–ZnO	RhB	38
Wang *et al.* 2023 (ref. 63)	$CuSbS_2$–CdS	RhB	22
Yan *et al.* 2011 (ref. 64)	$SnIn_4S_8$ microspheres	MO	14
Chen *et al.* 2009 (ref. 61)	$ZnIn_2S_4$ microspheres	MO	0.48
Cao *et al.* 2024 (ref. 65)	Zn-doped CuS	MB	75
El-Gendy *et al.* 2023 (ref. 66)	CuS modified TiO_2	MB	75
El-Gendy *et al.* 2023 (ref. 66)	MoS_2 modified TiO_2	MB	78
Sharkawy *et al.* 2023 (ref. 67)	MoS_2 and N modified TiO_2	MB	40

For the preparation of the structured samples, we used the EDE solvent mixture, as described above. To study possible differences induced from the solvent applied for the film preparation, we additionally analysed a planar thin film prepared from EDE. These investigations reveal similar characteristics to those of the thin films prepared from DCM including an isotropic mesophase formation around 145 °C and the near-range order observed at higher temperatures (see Fig. S15†). Compared to that, in the structured samples, this near-range order is not observed, which is not unexpected, due to the thin wall thicknesses of only 50–60 nm in the structured substrates (Fig. 4, bottom row). These differences can be also nicely seen by comparing the progression of the scattering patterns of the three films during the heating run shown in the ESI videos† (Video 1: planar DCM, Video 2: planar EDE and Video 3: structured EDE). Looking at the line-cuts in Fig. 5b, the mesophase shows a well observable peak up to 160 °C. At this temperature, the particle growth initiates rapidly, as evidenced by a pronounced increase in the GISAXS invariant $\bar{I}$ (Fig. 5a), while the peak originating from the mesophase persists as a broad shoulder in the line-cuts (Fig. 5b) up to a temperature of 317 °C. More details to the calculation of the GISAXS invariant and in-plane correlation length are given in the ESI.† Furthermore, a broad maximum in the GISAXS invariant is observed between 160 °C and 202 °C, matching the primary mass loss observed in the TGA measurements (Fig. 2a). Between 317 °C and 376 °C, the shoulder attributable to the mesophase gradually weakens and ultimately vanishes. Based on the TGA data of the EDE-based sample, which reveals a slight continuous mass loss up to these temperatures, we assume that at these temperatures the remaining decomposition products, which had formed the defined mesophase, evaporate creating the open micropore structure of the film. The discussed temperatures are marked with arrows of matching colors in Fig. 5a and b. The line-cuts at the same selected temperatures of the planar and structured EDE-based films are depicted in Fig. S16.† At higher temperatures around 300 °C, the correlation length increases in all three samples. This increase is very likely based on an Ostwald-ripening-type growth mechanism and more intense in the structured film compared to the planar films. This difference can be assigned to the additional decomposition of the polystyrene spheres in the structured film.[59] The growth data from $CuInS_2$ (ref. 52) and ZnS[50] in previous studies supports this assumption, with a similar loss in near-range order in the out-of-plane direction at higher temperatures.

Finally, the lateral size of the asymmetric micropores open parallel to the substrate (see above) was determined from the in-plane cuts of the GISAXS data (integration from $q_{min} = 0.1$ to $q_{max} = 4.18$ nm^{-1}) of the samples after the heating run. Therefore, a fitting function with structure factor (sticky hard-sphere model) and form factor (Schultz sphere particle distribution) contributions was applied. We provide further details to the used fitting function and the fitting process in the ESI (Fig. S17†). From the fitting function, we obtained Schultz sphere distributed micropore sizes around 1.6 nm for the planar film prepared from DCM as well as for the films prepared with the EDE solvent mixture (see Fig. S18†). The distances between the micropores, extracted from the same fitting function mentioned above, correspond to 6.2 – 8.5 nm (see also Fig. S18 and Table S5†).

To get more information about the micropores, we investigated the material with scanning transmission electron microscopy (STEM) in high-angle annular dark-field (HAADF) mode, further revealing its highly porous nature (Fig. 5c). With 2.6 ± 0.8 nm, the pore sizes agree well with the ones extracted from the GISAXS characterizations, considering the different techniques and their specific measurement uncertainties (ESI, Table S5†). Furthermore, we investigated the surface and porosity with BET N_2 gas adsorption of a $ZnIn_2S_4$ powder. These adsorption experiments revealed a surface area of 40.4 m^2 g^{-1} and BJH pore sizes around 2.4 nm, agreeing well with the previously discussed results (ESI, Fig. S19†).

Photocatalytic dye degradation of Rhodamine B

The hierarchical porosity greatly enhances the available surface area of the material, which is important for increasing the efficiency of heterogeneous catalysts. This does not only increase the number of available reaction sites, but also

decreases the charge transport distances within the material and thus reduces the charge recombination.

To investigate the photocatalytic activity of the hierarchically porous $ZnIn_2S_4$ films, we performed photocatalytic dye degradation experiments of Rhodamine B (RhB) under simulated sun light (the absorption of a typical $ZnIn_2S_4$ film is shown in Fig. S20†). The films were placed in a beaker filled with a 4 mg L^{-1} RhB solution. Because $ZnIn_2S_4$ has a similar absorption range as RhB, the films were placed about 0.5 cm below the surface, to achieve a good light harvesting. More details are given in the experimental part and in the ESI (Fig. S21†). The planar thin film shows comparable activity to similar experiments from the literature with heterogeneous dispersions, while the hierarchically structured film shows a 3.3 times higher specific activity as shown in Fig. 6 and Table 2.

Conclusions

In conclusion, we successfully prepared hierarchically porous zinc indium sulfide thin films with an improved surface to volume ratio due to the additional porosity. The macropores (~300 nm) are formed by microsphere lithography, combined with metal xanthate precursors creating the micropores (~2 nm) in the metal sulfide film during the conversion process. The polystyrene templates allow an easy control over the macropore sizes and can be thermally removed.

From the GIWAXS and XRD measurements, we suspect an initial zinc sulfide phase formation, which converts to zinc indium sulfide at higher temperatures. The GISAXS experiments showed minor structural changes in the films starting already at 110 °C, followed by the formation of an ordered mesophase, which can be associated with the micropore formation. The smaller pores were confirmed and characterized by fitting of the GISAXS data, BET N_2 adsorption and high-angle annular dark-field STEM measurements.

Photocatalytic dye degradation tests using Rhodamine B showed a more than 3.3-fold increase in specific catalytic activity of the hierarchically porous $ZnIn_2S_4$ films compared to a planar thin film, which we ascribe to (i) an increased number of available reaction sites at the surface, (ii) facilitated transport of the reactants and products to and away from the reaction sites, respectively, as well as (iii) reduced recombination in the photocatalyst due to decreased distances for charge carrier transport.

With this method for the formation of hierarchically porous thin films, we provide an accessible and tuneable possibility to improve the specific photocatalytic activity of metal sulfides. Preparing catalysts as porous thin films not only enhances the useable surface area, but also provides easy recyclability of the catalyst or incorporation in continuous flow reactors. Furthermore, the xanthate route provides a great range of different metal sulfide films to be fabricated and, therefore, the option for covering a variety of photocatalytic applications. For future work, we plan to optimize the catalyst even further *via* suitable co-catalysts to improve the activity and its stability as well as the adequate characterization in the hydrogen evolution reaction with water. Contrary to the Rhodamine B degradation, the water splitting reaction will be able to utilize the micropores more effectively as well.

Experimental section

The chemicals and solvents were purchased from commercial suppliers and used without further purification: dichloromethane (≥99.8%, Fisher Scientific), hydrochloric acid (37%, Fisher Scientific), absolute ethanol (Sigma Aldrich, ≥99.8%), polystyrene microspheres (Latex beads, LB3, 0.3 μm mean particle size), ethanolamine (≥99%, Sigma-Aldrich), diethyl ether (Sigma Aldrich), Rhodamine B (Fluka). Indium *O*-2,2-dimethylpentan-3-yl dithiocarbonate[52] was bought from Aglycon GmbH (synthesized according to a previous report[43]) and recrystallized from chloroform/methanol. Zinc *O*-pentan-1-yl dithiocarbonate was synthesized according to previous works.[50,54,55] Details of the metal xanthate synthesis are provided in the ESI.†

Preparation of the ZIS films

As precursor solutions, indium *O*-2,2-dimethylpentan-3-yl dithiocarbonate and zinc *O*-pentan-1-yl dithiocarbonate were dissolved in the respective solvents (DCM, ethanol : DCM : ethanolamine = EDE, 2-propanol : DCM : ethanolamine = PDE) to form 0.05 mM solutions. The solutions were combined to obtain the appropriate ratios of Zn : In (1.6–2.2). 100 μL of the precursor solutions were pipetted onto a substrate for the coating of the films. The structured samples were spin-coated with 5000 rpm for one minute and the planar films were spin coated with 1000 rpm (spin coater: WS-650MZ-23NPPB, Laurell Technologies).

Characterization methods

Thermogravimetric analysis. TGA experiments were performed with a TGA8000 from PerkinElmer with ceramic crucibles and a N_2 flow rate of 40 mL min^{-1}. The materials were investigated between 25 and 400 °C with a heating rate of 10 °C min^{-1}.

X-ray diffraction. Powder and film X-ray diffractograms were recorded with a Rigaku Miniflex 600 with a D/Tex Ultra detector using CuK_α radiation and the evaluation of the diffraction patterns was performed with the SmartLabStudioII software.

SEM. Scanning Electron Microscopy was performed with a TESCAN MIRA3 Field Emission Scanning Electron Microscope (FESEM) using an in-beam secondary electron detector. The device was operated at 5 kV. The samples were coated with a 10 nm chromium layer by thermal evaporation. The pore sizes and wall thicknesses were estimated with the freeware software Gwyddion 2.63. EDX spectra were recorded with an Octane Super detector from AMETEK EDAX and an energy of 15 kV.

Film thickness. The film thicknesses were measured with a DektakXT Profilometer from Bruker.

X-ray scattering experiments. GISAXS and GIWAXS measurements were performed at the Austrian SAXS Beamline 5.2 L of the electron storage ring Elettra (Italy).[68] The in-plane *q*-range was set up to 0.1 to 4.18 nm^{-1} for the GISAXS

measurements. This q-range ($q_{min} = 0.1$ and $q_{max} = 4.18$ nm^{-1}) was also used for the integration in the horizontal line-cuts at a vertical height of $q_z = 0.5$ nm^{-1}. The GIWAXS setup was adjusted for an angular range of 2θ of up to 44.9° (scattering vector $q = 4\pi/\lambda \sin(2\theta/2)$). All these experiments were carried out with a photon energy of 16 keV. The angular calibration of the detector for the GISAXS measurements was carried out using silver behenate powder (d-spacing of 58.38 Å) and for the GIWAXS measurements p-bromo benzoic acid was used for the calibration.

The samples were mounted on an Anton Paar DHS 1100 heating cell equipped with a specially designed dome with Kapton windows to provide high X-ray transmissivity with low background. The scattering data was recorded using a Pilatus3 1M detector. The sample chamber was purged with N_2 during the whole heating run experiments from 25 to 400 °C. During the heating run, one frame was recorded every 6 seconds to obtain a temperature resolution of 1 °C. For the GISAXS measurements an incident angle of 0.1° was chosen and for the GIWAXS measurements an angle of 0.55° was used.

TEM. STEM investigations were carried out on a probe corrected FEI Titan³ (Thermo Fisher Scientific, Eindhoven) operated at 300 kV with a field emission source (X-FEG) at a convergence angle of 19.6 mrad. The sample preparation was performed similar to the ZIS thin films, with a 0.05 mM precursor solution in EDE (1 : 1.8 Zn : In weight ratio). Only one drop of the precursor solution was put on a Ni TEM grid coated with a 30 nm amorphous carbon film and spin coated at 1000 rpm for 30 s.

BET N_2 gas adsorption. N_2 gas adsorption for determination of surface area and porosity of the powder sample was performed with a Micromeritics 3Flex at 77.043 K.

Photocatalytic dye degradation

For the photocatalysis experiments, the coated substrates were submerged in a 4 mg L^{-1} solution of Rhodamine B in deion. water for 30 min for an adsorption equilibrium to establish. Afterwards, the substrates were submerged in 75 mL of fresh Rhodamine B solution in a 150 mL beaker. The substrates were elevated on a scaffold assembled from glass slides to submerge the substrates approx. 0.5 cm below the surface (a detailed sketch is depicted in the ESI, Fig. S20†). All beakers were put under a simulated sun spectrum (100 mW cm^{-2}, Steuernagel KHS SC1200). A Rhodamine B solution without any photocatalyst was additionally measured as reference to subtract any non-catalyst related degradation. The absorptions of the solutions were measured with a Shimadzu UV-1800 spectrometer in the range of 400–650 nm to quantify the amount of degraded dye.

Data availability

The data underlying this study are available in the published article and its ESI.†

Author contributions

M. S.: conceptualization, data curation, formal analysis, synthesis and investigation, characterization methodology, project administration, visualization, writing – original draft, writing – review & editing. M. E.: conceptualization, data curation, investigation, writing – review & editing. F. W.: investigation (SEM), writing – review & editing. D. K.: investigation, data curation, review & editing. M. D.: investigation, data curation, review & editing. H. A.: conceptualization, funding acquisition, data curation & investigation (GISAXS/GIWAXS), writing – review & editing. G. T.: resources, supervision, funding acquisition, writing – review & editing. T. R.: conceptualization, funding acquisition, project administration, supervision, writing – original draft, writing – review & editing.

Conflicts of interest

There are no conflicts to declare.

Acknowledgements

The authors gratefully acknowledge Graz University of Technology for financing this work through the Lead Project Porous Materials@Work for Sustainability (LP-03). Additionally, the authors thank the CERIC-ERIC Consortium for the access to experimental facilities of the Austrian SAXS beamline at Elettra Sincrotrone Trieste as well as financial support. The authors further appreciate Simon Renner for conducting the BET adsorption measurements and moreover, the authors thank Elena Zuccala and Bettina Schlemmer for their help with the time resolved GIWAXS and GISAXS measurements.

References

1 J. Xue, H. Liu, S. Zeng, Y. Feng, Y. Zhang, Y. Zhu, M. Cheng, H. Zhang, L. Shi and G. Zhang, *Sol. RRL*, 2022, **6**, 2101042.
2 H. Xie, Y. Feng, X. He, Y. Zhu, Z. Li, H. Liu, S. Zeng, Q. Qian and G. Zhang, *Small*, 2023, **19**, e2207425.
3 H. Qian, Z. Liu, Z. Guo, M. Ruan and J. Ma, *J. Alloys Compd.*, 2020, **830**, 154639.
4 T. Yan, Q. Yang, R. Feng, X. Ren, Y. Zhao, M. Sun, L. Yan and Q. Wei, *Front. Environ. Sci. Eng.*, 2022, **16**, 131.
5 L. Yu, X. He, B. Peng, W. Wang, G. Wan, X. Ma, S. Zeng and G. Zhang, *Matter*, 2023, **6**, 1604–1621.
6 L. Yu, J. Li, G. Wang, B. Peng, R. Liu, L. Shi and G. Zhang, *ACS Appl. Mater. Interfaces*, 2021, **13**, 61116–61128.
7 P. Kulkarni, S. K. Nataraj, R. G. Balakrishna, D. H. Nagaraju and M. V. Reddy, *J. Mater. Chem. A*, 2017, **5**, 22040–22094.
8 T. Zhang, T. Wang, F. Meng, M. Yang and S. Kawi, *J. Mater. Chem. C*, 2022, **10**, 5400–5424.
9 Z. Chen, D. Li, Z. Wenjuan, Y. Shao, T. Chen, M. Sun and X. Fu, *J. Phys. Chem. C*, 2009, **113**, 4433–4440.
10 F. Fang, L. Chen, Y.-B. Chen and L.-M. Wu, *J. Phys. Chem. C*, 2010, **114**, 2393–2397.
11 J. Lee, H. Kim, T. Lee, W. Jang, K. H. Lee and A. Soon, *Chem. Mater.*, 2019, **31**, 9148–9155.

12 L. Wang, H. Zhou, H. Zhang, Y. Song, H. Zhang, L. Luo, Y. Yang, S. Bai, Y. Wang and S. Liu, *Nanoscale*, 2020, **12**, 13791–13800.
13 J. Zhao, X. Yan, N. Zhao, X. Li, B. Lu, X. Zhang and H. Yu, *RSC Adv.*, 2018, **8**, 4979–4986.
14 W. Pudkon, S. Kaowphong, S. Pattisson, P. J. Miedziak, H. Bahruji, T. E. Davies, D. J. Morgan and G. J. Hutchings, *Catal. Sci. Technol.*, 2019, **9**, 5698–5711.
15 X. Guo, Y. Peng, G. Liu, G. Xie, Y. Guo, Y. Zhang and J. Yu, *J. Phys. Chem. C*, 2020, **124**, 5934–5943.
16 L. Guo, X. Han, K. Zhang, Y. Zhang, Q. Zhao, D. Wang and F. Fu, *Catalysts*, 2019, **9**, 729.
17 C. Gnehm and A. Niggli, *J. Solid State Chem.*, 1972, **5**, 118–125.
18 Y. Chen, S. Hu, W. Liu, X. Chen, L. Wu, X. Wang, P. Liu and Z. Li, *Dalton Trans.*, 2011, **40**, 2607–2613.
19 M. A. Sriram, P. H. McMichael, A. Waghray and P. N. Kumta, *J. Mater. Sci.*, 1998, **33**, 4333–4339.
20 X. Yu, J. Liu, Y. Yu, S. Zuo and B. Li, *Carbon*, 2014, **68**, 718–724.
21 L. Shi, P. Yin and Y. Dai, *Langmuir*, 2013, **29**, 12818–12822.
22 C. Du, Q. Zhang, Z. Lin, B. Yan, C. Xia and G. Yang, *Appl. Catal., B*, 2019, **248**, 193–201.
23 M.-Q. Yang, Y.-J. Xu, W. Lu, K. Zeng, H. Zhu, Q.-H. Xu and G. W. Ho, *Nat. Commun.*, 2017, **8**, 14224.
24 S. Shen, L. Zhao and L. Guo, *J. Phys. Chem. Solids*, 2008, **69**, 2426–2432.
25 J. Shen, J. Zai, Y. Yuan and X. Qian, *Int. J. Hydrogen Energy*, 2012, **37**, 16986–16993.
26 H. Ye, H. Wang, B. Zhang, F. Zhao and B. Zeng, *Talanta*, 2018, **186**, 459–466.
27 J. Yang, D. Wang, H. Han and C. Li, *Acc. Chem. Res.*, 2013, **46**, 1900–1909.
28 J. Ran, J. Zhang, J. Yu, M. Jaroniec and S. Z. Qiao, *Chem. Soc. Rev.*, 2014, **43**, 7787–7812.
29 W. Y. Lim, M. Hong and G. W. Ho, *Dalton Trans.*, 2016, **45**, 552–560.
30 J. Zhao, X. Yan, N. Zhao, X. Li, B. Lu, X. Zhang and H. Yu, *RSC Adv.*, 2018, **8**, 4979–4986.
31 U. Daraz, T. M. Ansari, S. A. Arain, M. A. Mansoor and M. Mazhar, *J. Chem. Soc. Pak.*, 2020, **42**, 155–163.
32 M. Li, J. Su and L. Guo, *Int. J. Hydrogen Energy*, 2008, **33**, 2891–2896.
33 H. Sampath, T. I. Jayaraj, R. Oommen and U. R. Parthasarathy, *Emerging Mater. Res.*, 2015, **4**, 286–289.
34 L. Zhang, W. Zhang, H. Tao, G. Wang, J. Ma, Q. Wang, M. Tan and S. Xu, *CrystEngComm*, 2017, **19**, 3619.
35 L. Wu, M. Li, B. Zhou, S. Xu, L. Yuan, J. Wei, J. Wang, S. Zou, W. Xie, Y. Qiu, M. Rao, G. Chen, L. Ding and K. Yan, *Small*, 2023, **19**, 2303821.
36 W. Yang, B. Liu, T. Fang, W.-A. Jennifer, L. Christophe, Z. Li, X. Zhang and X. Jiang, *Nanoscale*, 2016, **8**, 18197.
37 H. Yu, X. Quan, Y. Zhang, N. Ma, S. Chen and H. Zhao, *Langmuir*, 2008, **24**, 7599–7604.
38 Y. Xie, Y. Liu, H. Cui, W. Zhao, C. Yang and F. Huang, *J. Power Sources*, 2014, **265**, 62–66.
39 C. Buchmaier, T. Rath, F. Pirolt, A.-C. Knall, P. Kaschnitz, O. Glatter, K. Wewerka, F. Hofer, B. Kunert, K. Krenn and G. Trimmel, *RSC Adv.*, 2016, **6**, 106120–106129.
40 E. Vakalopoulou, D. Knez, M. Sigl, G. Kothleitner, G. Trimmel and T. Rath, *ChemNanoMat*, 2023, **9**, e202200414.
41 T. Rath, J. M. Marin-Beloqui, X. Bai, A.-C. Knall, M. Sigl, F. G. Warchomicka, T. Griesser, H. Amenitsch and S. A. Haque, *ACS Appl. Mater. Interfaces*, 2023, **15**, 41624–41633.
42 T. Rath, A. J. MacLachlan, M. D. Brown and S. A. Haque, *J. Mater. Chem. A*, 2015, **3**, 24155–24162.
43 T. Rath, M. Edler, W. Haas, A. Fischereder, S. Moscher, A. Schenk, R. Trattnig, M. Sezen, G. Mauthner, A. Pein, D. Meischler, K. Bartl, R. Saf, N. Bansal, S. A. Haque, F. Hofer, E. J. List and G. Trimmel, *Adv. Energy Mater.*, 2011, **1**, 1046–1050.
44 M. Al-Shakban, P. D. Matthews and P. O'Brien, *Chem. Commun.*, 2017, **53**, 10058–10061.
45 P. D. McNaughter, S. A. Saah, M. Akhtar, K. Abdulwahab, M. Azad Malik, J. Raftery, J. A. M. Awudza and P. O'Brien, *Dalton Trans.*, 2016, **45**, 16345.
46 N. Pradhan, B. Katz and S. Efrima, *J. Phys. Chem. B*, 2003, **107**, 13843–13854.
47 M. D. Khan, M. A. Malik, J. Akhtar, S. Mlowe and N. Revaprasadu, *Thin Solid Films*, 2017, **638**, 338–344.
48 P. S. Nair, T. Radhakrishnan, N. Revaprasadu, G. Kolawole and P. O'Brien, *J. Mater. Chem.*, 2002, **12**, 2722–2725.
49 G. B. Shombe, M. D. Khan, C. Zequine, C. Zhao, R. K. Gupta and N. Revaprasadu, *Sci. Rep.*, 2020, **10**, 3260.
50 E. Vakalopoulou, T. Rath, M. Kräuter, A. Torvisco, R. C. Fischer, B. Kunert, R. Resel, H. Schröttner, A. M. Coclite, H. Amenitsch and G. Trimmel, *ACS Appl. Nano Mater.*, 2022, **5**, 1508–1520.
51 J. Yu, Q. Yan and D. Shen, *ACS Appl. Mater. Interfaces*, 2010, **2**, 1922–1926.
52 E. Vakalopoulou, T. Rath, F. G. Warchomicka, F. Carraro, P. Falcaro, H. Amenitsch and G. Trimmel, *Mater. Adv.*, 2022, **3**, 2884–2895.
53 P. Liu, L. Bai, J. Yang, H. Gu, Q. Zhong, Z. Xie and Z. Gu, *Nanoscale Adv.*, 2019, **1**, 1672–1685.
54 T. Ikeda and H. Hagihara, *Acta Crystallogr.*, 1966, **21**, 919–927.
55 T. C. Vagvala, S. S. Pandey, S. Krishnamurthy and S. Hayasa, *Z. Anorg. Allg. Chem.*, 2016, **642**, 134–139.
56 S. Dunst, T. Rath, A. Radivo, E. Sovernigo, M. Tormen, H. Amenitsch, B. Marmiroli, B. Sartori, A. Reichmann, A.-C. Knall and G. Trimmel, *ACS Appl. Mater. Interfaces*, 2014, **6**, 7633–7642.
57 L. Su, X. Ye, S. Meng, X. Fu and S. Chen, *Appl. Surf. Sci.*, 2016, **384**, 161–174.
58 L. Wei, Y. Chen, Y. Lin, H. Wu, R. Yuan and Z. Li, *Appl. Catal., B*, 2014, **144**, 521–527.
59 J. D. Peterson, S. Vyazovkin and C. A. Wight, *Macromol. Chem. Phys.*, 2001, **202**, 775–784.

60 E. Vakalopoulou, C. Buchmaier, A. Pein, R. Saf, R. C. Fischer, A. Torvisco, F. Warchomicka, T. Rath and G. Trimmel, *Dalton Trans.*, 2020, **49**, 14564–14575.
61 Z. Chen, D. Li, W. Zhang, Y. Shao, T. Chen, M. Sun and X. Fu, *J. Phys. Chem. C*, 2009, **113**, 4433–4440.
62 C. Tan, G. Zhu, M. Hojamberdiev, K. S. Lokesh, X. Luo, L. Jin, J. Zhou and P. Liu, *J. Hazard. Mater.*, 2014, **278**, 572–583.
63 W. Wang, Q. Sheng, G. Zhi, Y. Zhao, R. Qu, L. Sun and S. Zhang, *Appl. Surf. Sci.*, 2023, **639**, 158251.
64 T. Yan, L. Li, G. Li, Y. Wang, W. Hu and X. Guan, *J. Hazard. Mater.*, 2011, **186**, 272–279.
65 J. Cao, D. Zhang and H. Zhang, *Mater. Res. Bull.*, 2024, **179**, 112990.
66 R. A. El-Gendy, H. M. El-Bery, M. Farrag and D. M. Fouad, *Sci. Rep.*, 2023, **13**, 7994.
67 H. M. El Sharkawy, A. M. Shawky, R. Elshypany and H. Selim, *Sci. Rep.*, 2023, **13**, 8845.
68 H. Amenitsch, M. Rappolt, M. Kriechbaum, H. Mio, P. Laggner and S. Bernstorff, *J. Synchrotron Radiat.*, 1998, **5**, 506–508.